MNRAS 000, 1–6 (2019) Preprint 5 September 2019 Compiled using MNRAS LATEX style file v3.0

Constraining the Gravitational-Wave Afterglow From a Binary Neutron Star Coalescence

Sharan Banagiri,[1]★ Michael W. Coughlin,[2]†James Clark,[3] Paul D. Lasky,[4 5] M. A. Bizouard,[6] Colm Talbot,[4 5] Eric Thrane [4 5] and Vuk Mandic[1]

[1]School of Physics and Astronomy, University of Minnesota, Minneapolis, Minnesota 55455, USA
[2]Division of Physics, Math, and Astronomy, California Institute of Technology, Pasadena, CA 91125, USA
[3]Department of Physics, Georgia Institute of Technology, Atlanta, GA 30332, USA
[4]School of Physics and Astronomy, Monash University, Clayton, Victoria 3800, Australia
[5]OzGrav: The ARC Centre of Excellence for Gravitational-wave Discovery, Monash University, Clayton, Victoria 3800, Australia
[6]LAL, Univ. Paris-Sud, CNRS/IN2P3, Université Paris-Saclay, F-91898 Orsay, France

5 September 2019

ABSTRACT

Binary neutron star mergers are rich laboratories for physics, accessible with ground-based interferometric gravitational-wave detectors such as Advanced LIGO and Advanced Virgo. If a neutron star remnant survives the merger, it can emit gravitational waves that might be detectable with the current or next generation detectors. The physics of the long-lived post-merger phase is not well understood and makes modeling difficult. In particular the phase of the gravitational-wave signal is not well modeled. In this paper, we explore methods for using long duration post-merger gravitational-wave signals to constrain the parameters and the properties of the remnant. We develop a phase-agnostic likelihood model which uses only the spectral content for parameter estimation and demonstrate the calculation of a Bayesian upper limit in the absence of a signal. With the millisecond magnetar model, we show that for an event like GW170817, the ellipticity of a long-lived remnant can be constrained to less than about 0.5 in the parameter space used.

Key words: gravitational waves, stars: neutron, methods: statistical

1 INTRODUCTION

The detection of gravitational-wave signals from binary black hole mergers (Abbott, B. P. et al 2016; Abbott, B. P. et al. 2017a; Abbott et al. 2018), and the binary neutron star merger GW170817 (Abbott et al. 2017a) by Advanced LIGO and Advanced Virgo (Aasi et al. 2015; Acernese et al. 2015) in their first and second observing runs (O1 and O2) show that compact binary coalescences are primary sources of gravitational waves (GW) for terrestrial gravitational-wave detectors. Binary neutron star mergers in particular provide an extremely rich environment for studying physics at conditions unattainable on Earth.

Searches by LIGO scientific collaboration and the Virgo collaboration following GW170817 did not find any evidence for gravitational waves from a neutron star remnant (Abbott et al. 2017c, 2019c,b,a), although there has been a claim for evidence of short-duration post-merger signal (van Putten & Della Valle 2019). The nature of the remnant in a binary neutron star coalescence depends on the mass and spin of the remnant and the nuclear equation of state(for e.g. Baiotti & Rezzolla (2017); Piro et al. (2017)). One possible outcome is the formation of a rapidly rotating, highly magnetized and long-lived ($t \geqslant 10$ s) massive neutron star (NS). Although no conclusive evidence for a long-lived remnant was found following GW170817, observations of X-ray afterglows of short gamma-ray bursts support this evolutionary pathway for a relatively large fraction of mergers (e.g., Rowlinson et al. 2013). Observations of GWs from a long-lived post-merger remnant could help probe the complex physics governing the pre and post-merger phase, as well as help constrain the equation of state of massive remnants. Some predictions of GW signals from long-lived remnants suggest they may be observable with second-generation observatories out to 40 Mpc (for e.g. Dall'Osso et al. (2015)), although more realistic analyses that account for the energy budget (Sarin et al. 2018) are more pessimistic and suggest that they might only be detectable with third-generation GW detectors Punturo et al. (2010); Hild et al. (2011).

There has been much work in exploring the GW emission from newly born magnetars. The nature of these GWs can depend sensitively on a number of aspects of neutron-star physics, including early cooling before transition to superfluidity, the effect of the magnetic field on the equilibrium shape, the internal dynamical state of a fully degenerate, oblique rotator, and the strength of the electromagnetic torque on the newly-born NS (e.g. Cutler (2002);

★ E-mail: banag002@umn.edu
† Email: mcoughli@caltech.edu

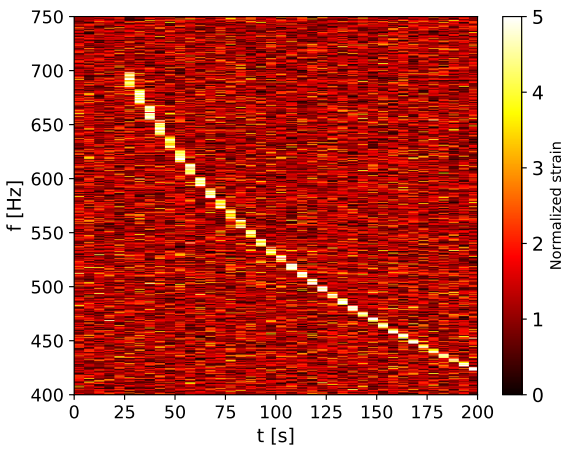

Figure 1. A normalized strain time-frequency map made with simulated Gaussian data recolored with O2 noise. A loud signal has been added for demonstration. The duration of each fast Fourier transform is 4 seconds and the entire map is 200 seconds long.

Dall'Osso et al. (2015); Doneva et al. (2015); Lasky & Glampedakis (2016)). The amplitudes and phases of the GWs depend on the complicated details of these physical mechanisms, which makes modeling and hence astrophysical inference from GW detections difficult. While there exists unmodeled Bayesian inference pipelines like Bayeswave (Cornish & Littenberg 2015; Chatziioannou et al. 2017) - which fits any signal using a wavelet expansion of variable dimensions - such analysis can be computationally expensive for long-transient signals considered in this paper.

In this Letter, we develop methods for Bayesian inference of long-transient signals which are robust towards some modelling uncertainties. We focus on the phase of the signal in particular and derive phase-agnostic likelihoods which depend only on the spectral content of the signal. We use this likelihood in the context of Bayesian parameter estimation to constrain intrinsic properties of a (long-lived) remnant such as ellipticity and the braking index, using the millisecond magnetar model waveform (Lasky et al. 2017; Sarin et al. 2018) as an example waveform. We note that while we use this waveform model to study and develop parameter-estimation methods, we do not claim that this is a realistic model of long-lived post-merger emission. We show how this formalism performs both in the presence and the absence of a signal and how upper limits can be placed on gravitational-wave emission in the case of non-detection.

2 MILLISECOND MAGNETAR MODEL

The search for post-merger emission from GW170817 by LIGO and Virgo (Abbott et al. 2017c, 2019c) considered a variety of possible signals, ranging from sub-second to hour-long timescales. In particular, the search for a signal from a long-lived remnant was based on a model derived from the dynamics of a spinning down neutron stars proposed by Sarin et al. (2018) and Lasky et al. (2017). This model - hear-after referred to as the millisecond magnetar model - derives the frequency evolution of the waveform from a spinning-down nascent neutron star with an arbitrary but fixed braking index n. We reproduce some of the details of the model below.

We assume that the rotational evolution of the star is described by the torque equation: $\dot{\Omega} \propto \Omega^n$, where Ω is the star's angular frequency. We also assume quadrupole GW emission caused by a non-zero ellipticity of the neutron star, so that $f(t) = \Omega(t)/\pi$. Integrating the torque equation yields the GW frequency:

$$f(t) = f_0 \left(1 + \frac{t - t_0}{\tau}\right)^{1/(1-n)}, \quad t \geqslant t_0. \tag{1}$$

Here t_0 is the start time of the emission (with some definition of $t = 0$), f_0 is the initial GW frequency (at $t = t_0$) and τ is the spin-down timescale. Equation 1 can describe emission from a variety of physical processes responsible for spin-down. For example, $n = 3$ describes magnetic dipole powered spin-down in vaccum, while $n = 5$ describes spin-down powered by emission of quadrupolar gravitational waves. The amplitude of the GW signal decreases with time as

$$h(t) = h_0 \left(1 + \frac{t - t_0}{\tau}\right)^{2/(1-n)}, \tag{2}$$

where we define an amplitude parameter h_0 as

$$h_0 = \frac{4\pi^2 G}{c^4} \frac{I_{zz}\epsilon}{d} f_0^2. \tag{3}$$

Here, d is the distance of the source, I_{zz} is the moment of inertia and ϵ is the eccentricity of the neutron star.

3 LIKELIHOOD MODEL

A common way to search for GW sources that are difficult to accurately model is to look for excess power in time-frequency representations (tf-maps) of GW detector data (Anderson et al. 2001; Sutton P. et al. 2010; Klimenko S., Yakushin I., Mercer A., and Mitselmakher G. 2008; Thrane et al. 2011). To detect GWs, the tf-maps are parsed by pattern-recognition algorithms looking for statistically significant clusters of pixels — for example, seeded (Prestegard & Thrane Prestegard & Thrane; Khan & Chatterji Khan & Chatterji) and seedless (Thrane & Coughlin 2013, 2014; Coughlin et al. 2014) clustering algorithms using predefined templates have been widely used in the past. In this paper, we use tf-maps of discrete (complex) Fourier transforms of the data, normalized by the noise power spectral density (PSD). An example map with a loud simulated signal is shown in Figure 1.

The likelihood model we start with assumes that the residual noise when the signal is subtracted from the data is colored Gaussian noise. The Gaussian likelihood for a pixel in tf-map is given by (Veitch et al. 2015) [1] :

$$\mathcal{L}(\tilde{d}_{ij}|\boldsymbol{\theta}) = \frac{2}{\pi T S^n_{ij}} \exp\left(-\frac{2}{T}\frac{|\tilde{d}_{ij} - \tilde{h}_{ij}(\boldsymbol{\theta})|^2}{S^n_{ij}}\right), \tag{4}$$

where i, j are indices for the pixel at the i-th time-segment and j-th frequency bin of the tf-map. The terms $\tilde{d}_{ij}$, $\tilde{h}_{ij}$ and S^n_{ij} are the Fourier transform of the data, the signal model and the noise PSD in the pixel i, j respectively. The term T is the duration of the data used

[1] We note here that the correct normalization of the Gaussian likelihood function in the frequency domain should be proportional to σ^{-2}, and not to σ^{-1} like in real time domain data. This is because frequency domain noise is generally complex in which both the real and imaginary parts of the noise are independently Gaussian. See Appendix D of Romano & Cornish (2017) for a careful examination of this.

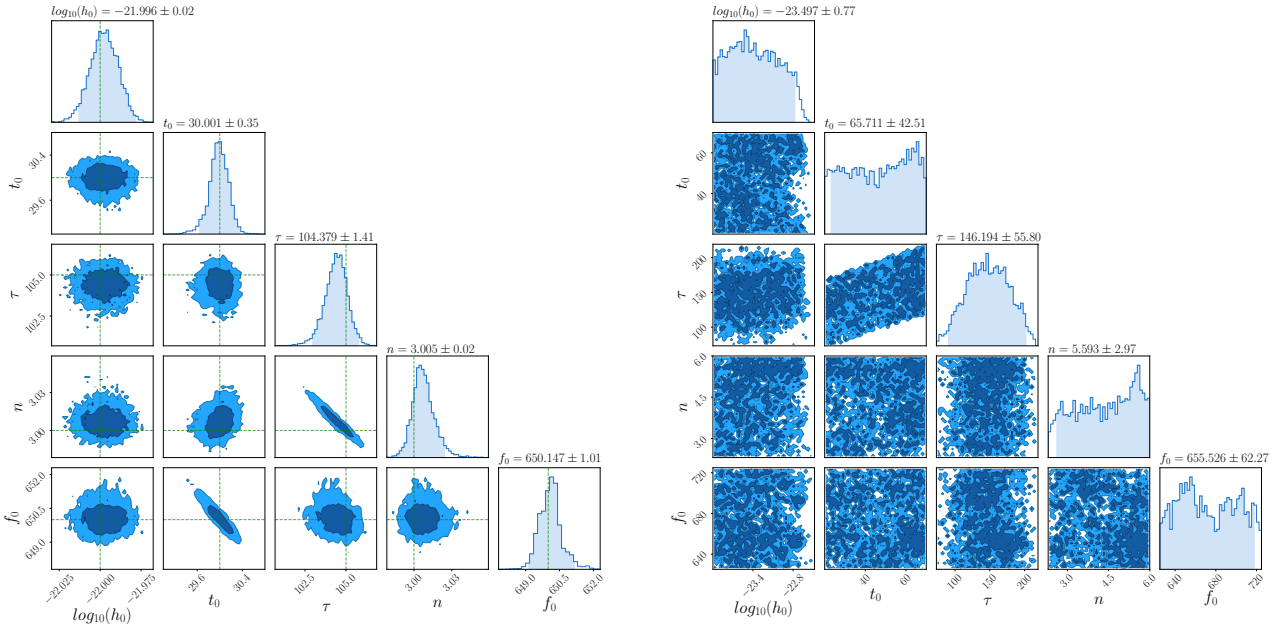

(a) (b)

Figure 2. Posteriors for a millisecond magnetar model simulation based on Eq 1. The colored regions in the 1-d posteriors show 95% confidence intervals. The vertical green lines in the left panel are the true values corresponding to $log_{10}(h_0) = -22.0$, $t_0 = 30\,s$, $\tau = 105\,s$, $n = 3$ and $f_0 = 650$ Hz from left to right. The dark and the light regions in the 2-d posteriors are 68% and 95% confidence levels respectively. The posteriors on the right for Gaussian noise when no signal is present.

for the Fourier transform, and $\boldsymbol{\theta}$ is the vector of model parameters. We point to Thrane & Talbot (2019) for a review of methods of Bayesian inference used in gravitational-wave astrophysics.

Given the uncertainty in the physics of the post-merger model describing the phase evolution of the remnants, we do not expect the signal to be accurate. Therefore we need to incorporate our ignorance of the true phase of the signal when analyzing the data. One way to do this is by marginalizing the phase of each pixel independently of other pixels[2]. The resultant phase marginalized likelihood depends only on the spectral content of the signal, and can be written as

$$\mathcal{L}_\phi(\tilde{d}_{ij}|\bar{\theta}) = \frac{2}{\pi T S^n_{ij}} \exp\left(-\frac{2}{T}\frac{|\tilde{d}_{ij}|^2 + |\tilde{h}_{ij}|^2}{S^n_{ij}}\right) \times I_0\left[\frac{4}{T}\frac{|\tilde{d}_{ij}||\tilde{h}_{ij}|}{S^n_{ij}}\right], \tag{5}$$

where $I_0(x)$ is the zeroth-order modified Bessel function of the first kind. We refer the reader to Supplementary material for the derivation of Eq. 5. This likelihood is for a single pixel of one interferometer. We take the product of likelihoods over all pixels to extend it over the entire tf-map. The simplest way to incorporate multiple detectors is to take the product of likelihoods for each detector:

$$\mathcal{L}(\{d_k\}|\boldsymbol{\theta}) = \prod_{i,j,k} \mathcal{L}_\phi(d_{ijk}|\boldsymbol{\theta}), \tag{6}$$

where k is an index over interferometers.

Tests of the likelihood in Eq. 5 show that the recovered parameters suffer from biases unless the exact spectrum of the noise is known. A common way to estimate the noise PSD is by calculating the mean of the PSDs of neighbouring or off source data segments. This estimate has a variance about the true PSD of the noise, which would need to be accounted for when large amounts of data are analyzed. One way to do this is to marginalize over the true PSD in a pixel given our measurement of S^n_{ij}. Starting with the Gaussian likelihood in Eq. 4 and using a χ^2 prior for the true PSD gives a likelihood based on a Student-t distribution for each pixel:

$$\mathcal{L}_S(\tilde{d}_{ij}|\bar{\theta}) = \frac{4\,\Gamma\left(1+\frac{\nu}{2}\right)}{\pi T \nu S^n_{ij}\,\Gamma(\nu/2)}\left[1 + \frac{4}{T}\frac{|\tilde{d}_{ij} - \tilde{h}_{ij}|^2}{\nu\, S^n_{ij}}\right]^{-(1+\frac{\nu}{2})}. \tag{7}$$

Here ν is the number of degrees of freedom of the χ^2 prior. A natural value for ν is $\nu = 2N$, where N is the number of data segments used to calculate S^n_{ij}. As pointed out in Rover et al. (2011), fewer degrees of freedom could be used, resulting in Student-t distributions with larger tails which are useful for robust inference in the presence of non-Gaussian artifacts in the data. We find that using fewer degrees of freedom gives better inferences; we estimate the PSD using $N = 40$ segments, and use $\nu = N$ in all the examples shown in this paper.

Having corrected for the PSD variance, we marginalize over the phase of the signal tf-map again to obtain a likelihood functions

[2] The phase marginalization being done here is different from the one used in parameter estimation analysis of compact binary coalescence , e.g Veitch et al. (2015). The phase evolution of compact binary waveforms is well understood, and it is only the initial phase which is marginalized over.

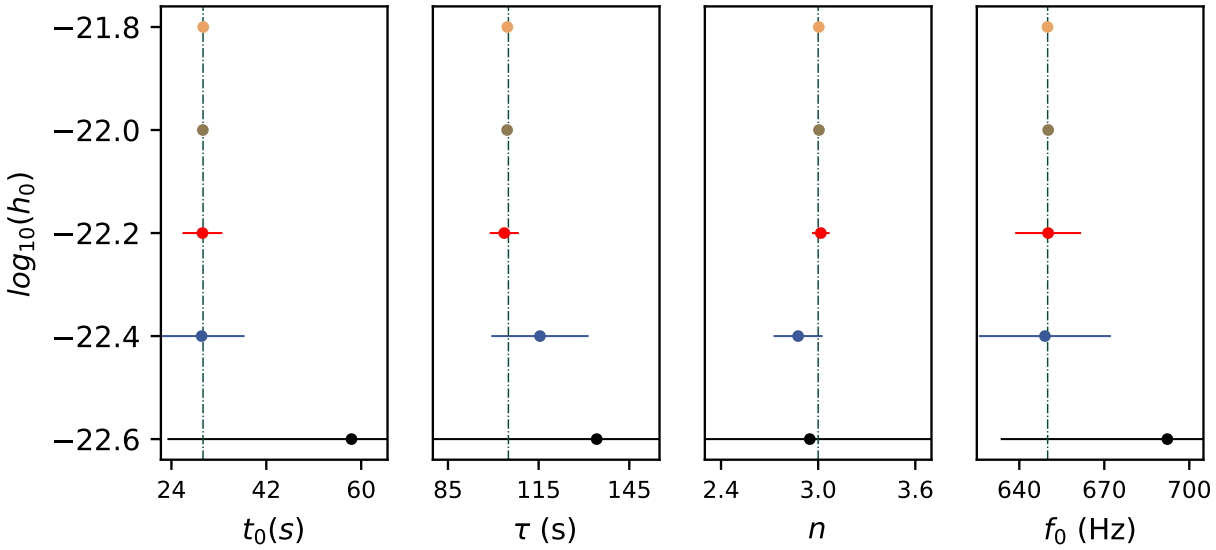

Figure 3. Posterior recoveries for the millisecond magnetar model showing the levels at which spectral parameters are constrained at different amplitude values. The vertical axis on the left shows the amplitude values used for the simulations. The solid dots are the maximum a posteriori values and the error bars correspond to 95% confidence levels. The vertical dashed-dotted line are the true values. Note that the x axis for these plots do not show to the full prior range and we have zoomed in to see the error bars better.

based on hyper-geometric functions for each pixel:

$$\mathcal{L}_{S,\phi}(\tilde{d}_{ij}|\bar{\theta}) = \frac{\alpha_{ij}}{2}(1-\beta_{ij})^{\gamma}\,{}_2F_1\left(0.5, -\gamma, 1, \frac{2\beta_{ij}}{\beta_{ij}-1}\right) + \frac{\alpha_{ij}}{2}(1+\beta_{ij})^{\gamma}\,{}_2F_1\left(0.5, -\gamma, 1, \frac{2\beta_{ij}}{\beta_{ij}+1}\right), \quad (8)$$

where,

$$\alpha_{ij} = \frac{2\,\Gamma\left(1+\frac{\nu}{2}\right)}{\pi\nu S^n_{ij}\,\Gamma(\nu/2)}\left[\frac{\nu\, S^n_{ij} + |\tilde{d}_{ij}|^2 + |\tilde{h}_{ij}|^2}{\nu\, S^n_{ij}}\right]^{-(1+\frac{\nu}{2})}, \quad (9)$$

$$\beta_{ij} = \frac{2\,|d_{ij}||h_{ij}|}{|d_{ij}|^2 + |h_{ij}|^2 + \nu S^n_{ij}},\ \gamma = -\left(1+\frac{\nu}{2}\right).$$

We point the reader again to the Supplementary material for the derivation and more details about both Eq. 7 and Eq. 8.

4 ANALYSIS

We now use the likelihood in Eq. 8 to recover a simulated signal from the millisecond magnetar model added to Gaussian noise colored with the O2 PSD of Hanford and Livingston Advanced LIGO detectors. We make tf-maps which are 200 seconds long, divided into 4 s Tukey-windowed FFT pixels. In this analysis, we assume that we know the distance d and the sky-location of the remnant, which were simulated to be the same as GW170817 and its electromagnetic counterpart (Abbott, B. P. et al. 2017b; Abbott et al. 2017b), i.e (ra, decl) = (13.1634 Hrs, −23.3185°) and d = 40 Mpc.

We sample over the five-dimensional parameter space $\boldsymbol{\theta} = \{h_0, t_0, \tau, n, f_0\}$ using PyMultiNest (Buchner et al. 2014), a python wrapper for the Nested Sampling implementation of MultiNest (Feroz et al. 2009). We use flat priors for all parameters [3] except h_0, for which we use a uniform in log prior from 10^{-24} to 10^{-21}. The left panel of Figure 2 shows an example of the parameter estimation of a simulated signal. In this case, the parameters are constrained roughly to a percent level.

The right panel of Figure 2 shows results from an analysis with Gaussian noise. In the absence of a signal, the posterior of the signal amplitude h_0 can be used to place upper limits on some properties of the remnant. Here, we get a 95% upper limit on h_0 of 2.1×10^{-23} with a uniform in log prior. Using the posterior samples and with Eq. 3, we can constrain the physical parameters of the remnants. In this case for example assuming a distance of 40 Mpc and the same fiducial moment of inertia as in Ref. (Abbott et al. 2019c) of $I_{zz} = 4.34\times10^{38}$ kg m^2, we get a 95% limit on ellipticity of 0.499. In reality we might not know the distance and the sky-position in the absence of an electromagnetic counterpart, and the moment of inertia of the remnant would also not be known precisely. These extra sources of uncertainty would need to be folded into both the analysis and the upper-limit calculation, either as extra parameters or using constraints from other measurements (for e.g. the distance measurement from the inspiral signal).

The upper limit on h_0 is also consistent with Figure 3, where we attempt to recover the simulated signals different amplitude levels while keeping constant the spectral parameters. The figure shows 95% confidence intervals with which the spectral parameters are recovered at different amplitudes. While the posteriors are well constrained for $h_0 \geqslant 4.0\times10^{-23}$, for a signal with amplitude $h_0 \leqslant 2.5\times10^{-23}$, the posteriors span almost the entire prior range.

We finally use the marginalized likelihood model on simulated signals with incorrect phase evolution models. We first test this in the frequency-domain with phase-scrambled maps — which are tf-

[3] The priors extend from 20s to 70s for t_0,from 2.3 to 5 on n, and from 625 Hz to 725 Hz on f_0. The parameter τ is degenerate with t_0, so in place of τ we actually sample over $T = \tau + t_0$ with a flat prior between 50s to 150s.

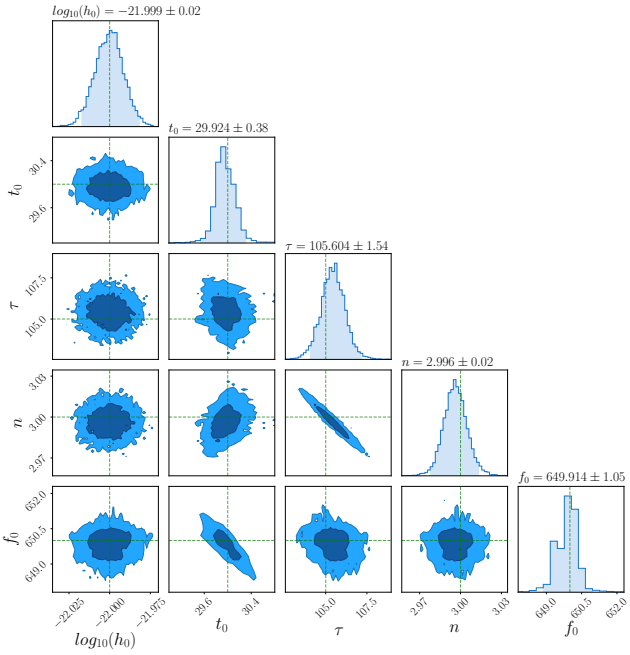

Figure 4. Posteriors recoveries for a simulation with small fluctuations added to the phase evolution. The colored regions in the 1-d posteriors show 95% confidence intervals. The vertical green lines in the left panel are the true values corresponding to $log_{10}(h_0) = -22.0, t_0 = 30\,s, \tau = 105\,s, n = 3$ and $f_0 = 650$ Hz from left to right. The dark and the light regions in the 2-d posteriors are 68% and 95% confidence levels respectively.

maps with random fluctuations added to the phase of each pixel. We find that the recovered posteriors are consistent with the true values, as expected for this statistic. We also perform a similar test by adding fluctuations to the time-domain phase evolution of the signal. We note that care is needed in the time-domain that the fluctuations not be large enough to affect the frequency evolution in the signal. The Figure 4 show the results for a signal with small fluctuations added in the time-domain, which demonstrate posterior recoveries consistent with the true parameters of the model.

5 CONCLUSION

Post-merger signals from neutron stars are a promising source of GWs for second and third generation gravitational-wave detectors. In this paper, we have described the application of a Bayesian likelihood formalism to the characterization of long-duration post-merger signals from binary neutron star mergers. We showed that this formalism is robust against fluctuations in phase evolution and is capable of constraining and measuring important astrophysical parameters like the spin, the braking index, moment of inertia and the eccentricity of magnetars. We note in particular the possibility to estimate the braking index of the remnant NS with gravitational-wave data. There have been only two measurements of braking indices of millisecond magnetars to date using, x-ray observations following short gamma-ray bursts (Lasky et al. 2017). Braking index measurements would be of particular interest since that gives direct information of the underlying mechanics of the spin-down. In conjugation with on-going developments (Takami et al. 2014; Bernuzzi et al. 2015; Tsang et al. 2019) in modeling of post-merger GW emission, parameter estimation methods can also help constrain the nuclear equation of state at very high densities.

As the second-generation gravitational-wave detectors progress towards their design sensitivity, it is plausible that there will be a detection of a long-transient gravitational-wave signal in the coming observing runs. In addition to post-merger searches, analyses of these signals also benefit from development of parameter estimations methods which make minimal model assumptions. We are planning further developments of robust methods of sky localization for transients which is especially important. One assumption we have made throughout this work is that the spectral model is well known. We are also developing parameter estimation methods which can handle a wider range of model uncertainties, and help in extracting astrophysical information from future detections.

ACKNOWLEDGEMENTS

We are grateful to Ling Sun, Joe Romano, David Keitel and Paul Schale and for useful discussion and comments. SB acknowledges support by the Hoff Lu Fellowship at the university of Minnesota, and by NSF grant PHY-1806630. MC is supported by the David and Ellen Lee Postdoctoral Fellowship at the California Institute of Technology. PDL is supported by ARC Future Fellowship FT160100112 and ARC Discovery Project DP180103155. ET and CT are supported by CE170100004. ET is supported by FT150100281. The authors are thankful for the computing resources provided by LIGO Laboratory. LIGO was constructed by the California Institute of Technology and Massachusetts Institute of Technology with funding from the National Science Foundation and operates under cooperative agreement PHY-0757058. All posterior corner plots were made with ChainConsumer (Hinton 2016). The code for the analysis in this paper is available upon request. A public release is being planned for the near future. This paper has been assigned document number LIGO-P1900107.

APPENDIX A: PHASE MARGINALIZED LIKELIHOOD

We derive Eq. 5 the phase marginalized Bessel function likelihood. We begin with Eq. 4 and write it by explicitly separating the phase term as,

$$\mathcal{L}(\tilde{d}_{ij}|\bar{\theta}, \phi^h_{ij}) = \frac{2}{\pi T S^n_{ij}} \exp\left(-\frac{2}{T}\frac{|\tilde{d}_{ij}|^2 + |\tilde{h}_{ij}|^2}{S^n_{ij}}\right) \times \exp\left(\frac{4}{T}\frac{|\tilde{d}_{ij}||\tilde{h}_{ij}|\cos(\phi^d_{ij} - \phi^h_{ij})}{S^n_{ij}}\right), \quad \text{(A1)}$$

where ϕ^h_{ij} and ϕ^d_{ij} are the model and data phase in the pixel i, j. We marginalize over ϕ^h_{ij} (or over $\phi_{ij} = \phi^d_{ij} - \phi^h_{ij}$) with a uniform prior as a natural choice. The marginalization integral is,

$$I^{\phi}_{ij} = \frac{1}{2\pi}\int_0^{2\pi} d\phi \exp\left(\frac{4}{T}\frac{|\tilde{d}_{ij}||\tilde{h}_{ij}|}{S^n_{ij}}\cos\phi\right). \quad \text{(A2)}$$

The integral can be described in terms of a zeroth-order mod-

ified Bessel function of the first kind (Arfken 2012), such the marginalized likelihood is,

$$\mathcal{L}_\phi(\tilde{d}_{ij}|\bar{\theta}) = \frac{2}{\pi T S^n_{ij}} \exp\left(-\frac{2}{T}\frac{|\tilde{d}_{ij}|^2 + |\tilde{h}_{ij}|^2}{S^n_{ij}}\right) \times I_0\left[\frac{4}{T}\frac{|\tilde{d}_{ij}||\tilde{h}_{ij}|}{S^n_{ij}}\right]. \tag{A3}$$

APPENDIX B: PHASE AND PSD MARGINALIZED LIKELIHOOD

A common way to estimate the noise PSD at some frequency is by averaging over the PSDs estimate from N neighbouring time segments:

$$S_{avg} = \frac{1}{N}\sum_i^N S_i. \tag{B1}$$

In the frequency domain, both the real and imaginary parts of the noise are assumed to be drawn from a colored Gaussian noise. If the true PSD is S, then the expectation value of both the real and imaginary part of the noise is $S/2$. Then the following sum follows a χ^2 distribution with $2N$ degrees of freedom:

$$\frac{2}{S}\sum_i^N S_i = \frac{2N}{S} S_{avg}. \tag{B2}$$

In general if some data $X \sim N(0, \sigma^2)$ and $\nu Y^2/\sigma^2 \sim \chi^2_\nu$, where Y is an estimator for σ, then the random variable $t = X/Y$ will form a Student-t distribution with ν degrees of freedom (James 2006). Using that here, we get the PSD marginalized likelihood for a pixel:

$$\mathcal{L}_S(\tilde{d}_{ij}|\bar{\theta}) = \frac{4\,\Gamma\left(1+\frac{\nu}{2}\right)}{\pi T \nu S^n_{ij}\,\Gamma(\nu/2)}\left[1 + \frac{4}{T}\frac{|\tilde{d}_{ij} - \tilde{h}_{ij}|^2}{\nu\, S^n_{ij}}\right]^{-(1+\frac{\nu}{2})}, \tag{B3}$$

with the natural choice of $\nu = 2N$. Note that since we start with the complex Gaussian distribution Eq. 4, the exponent is not $-(\nu+1)/2$ and so this is not an exact Student-t distribution in $|\tilde{d}_{ij} - \tilde{h}_{ij}|$. Now we marginalize over the phase. We define the α_{ij},β_{ij} and γ variables as in Eq. 9 which allows us to write the likelihood as,

$$\mathcal{L}^{ij}_S(\tilde{d}_{ij}|\bar{\theta}) = \alpha_{ij}\left[1 - \beta_{ij}\cos(\phi^s_{ij} - \phi^h_{ij})\right]^\gamma. \tag{B4}$$

We now marginalize over the phase term $\phi_{ij} = \phi^s_{ij} - \phi^h_{ij}$;

$$\mathcal{L}^{ij}_S(\tilde{d}_{ij}|\bar{\theta}) = \frac{\alpha_{ij}}{2\pi}\int_0^{2\pi} d\phi_{ij}\left[1 - \beta_{ij}\cos\phi_{ij}\right]^\gamma \tag{B5}$$

The integral can be written in terms of Gauss hypergeometric functions as,

$$\mathcal{L}^{ij}_S(\tilde{d}_{ij}|\bar{\theta}) = \frac{\alpha_{ij}}{2}(1-\beta_{ij})^\gamma\, {}_2F_1\left(0.5, -\gamma, 1, \frac{2\beta_{ij}}{\beta_{ij}-1}\right) + \frac{\alpha_{ij}}{2}(1+\beta_{ij})^\gamma\, {}_2F_1\left(0.5, -\gamma, 1, \frac{2\beta_{ij}}{\beta_{ij}+1}\right), \tag{B6}$$

which gives the phase and PSD marginalized likelihood for each pixel.

REFERENCES

Aasi J., et al., 2015, Class. Quant. Grav., 32, 074001
Abbott, B. P. et al 2016, Phys. Rev. Lett., 116, 061102
Abbott, B. P. et al. 2017a, Phys. Rev. Lett., 119, 141101
Abbott, B. P. et al. 2017b, Phys. Rev. Lett., 119, 161101
Abbott B. P., et al., 2017a, Phys. Rev. Lett., 119, 161101
Abbott B. P., et al., 2017b, Astrophys. J., 848, L12
Abbott B. P., et al., 2017c, Astrophys. J., 851, L16
Abbott B. P., et al., 2018 (arXiv:1811.12907)
Abbott B. P., et al., 2019a (arXiv:1908.01012)
Abbott B. P., et al., 2019b, Phys. Rev., X9, 011001
Abbott B. P., et al., 2019c, The Astrophysical Journal, 875, 160
Acernese F., et al., 2015, Class. Quant. Grav., 32, 024001
Anderson W. G., Brady P. R., Creighton J. D. E., Flanagan E. E., 2001, Phys. Rev., D63, 042003
Arfken G., 2012, Mathematical Methods for Physicists. Elsevier, doi:https://doi.org/10.1016/C2009-0-30629-7
Baiotti L., Rezzolla L., 2017, Rept. Prog. Phys., 80, 096901
Bernuzzi S., Dietrich T., Nagar A., 2015, Phys. Rev. Lett., 115, 091101
Buchner J., et al., 2014, Astronomy and Astrophysics, 564, A125
Chatziioannou K., Clark J. A., Bauswein A., Millhouse M., Littenberg T. B., Cornish N., 2017, Phys. Rev., D96, 124035
Cornish N. J., Littenberg T. B., 2015, Class. Quant. Grav., 32, 135012
Coughlin M., Thrane E., Christensen N., 2014, Phys. Rev. D, 90, 083005
Cutler C., 2002, Phys. Rev. D, 66, 084025
Dall'Osso S., Giacomazzo B., Perna R., Stella L., 2015, The Astrophysical Journal, 798, 25
Doneva D. D., Kokkotas K. D., Pnigouras P., 2015, Phys. Rev. D, 92, 104040
Feroz F., Hobson M. P., Bridges M., 2009, Mon. Not. Roy. Astron. Soc., 398, 1601
Hild S., et al., 2011, Classical and Quantum Gravity, 28, 094013
Hinton S. R., 2016, The Journal of Open Source Software, 1, 00045
James F., 2006, Statistical Methods in Experimental Physics, 2nd edn. WORLD SCIENTIFIC, p. 75 (https://www.worldscientific.com/doi/pdf/10.1142/6096), doi:10.1142/6096, https://www.worldscientific.com/doi/abs/10.1142/6096
Khan R., Chatterji S., ,] 10.1088/0264-9381/26/15/155009, 26, 155009
Klimenko S., Yakushin I., Mercer A., and Mitselmakher G. 2008, Class. Quant. Grav., 25, 114029
Lasky P. D., Glampedakis K., 2016, Mon. Not. R. Astron. Soc., 458, 1660
Lasky P. D., Leris C., Rowlinson A., Glampedakis K., 2017, ApJL, 843, L1
Piro A. L., Giacomazzo B., Perna R., 2017, Astrophys. J., 844, L19
Prestegard Thrane, LIGO-L1200204-v1: Burstegard: a hierarchical clustering algorithm, https://dcc.ligo.org/LIGO-L1200204/public
Punturo M., et al., 2010, Classical and Quantum Gravity, 27, 084007
Romano J. D., Cornish N. J., 2017, Living Rev. Rel., 20, 2
Rover C., Meyer R., Christensen N., 2011, Class. Quant. Grav., 28, 015010
Rowlinson A., O'Brien P. T., Metzger B. D., Tanvir N. R., Levan A. J., 2013, MNRAS, 430, 1061
Sarin N., Lasky P. D., Sammut L., Ashton G., 2018, Phys. Rev., D98, 043011
Sutton P. et al. 2010, New Journal of Physics, 12, 053034
Takami K., Rezzolla L., Baiotti L., 2014, Phys. Rev. Lett., 113, 091104
Thrane E., Coughlin M., 2013, Phys. Rev. D, 88, 083010
Thrane E., Coughlin M., 2014, Phys. Rev. D, 89, 063012
Thrane E., Talbot C., 2019, Publications of the Astronomical Society of Australia, 36, e010
Thrane E., Kandhasamy S., Ott C. D., et al., 2011, Phys. Rev. D, 83, 083004
Tsang K. W., Dietrich T., Van Den Broeck C., 2019 (arXiv:1907.02424)
Veitch J., et al., 2015, Phys. Rev., D91, 042003
van Putten M. H. P. M., Della Valle M., 2019, Mon. Not. Roy. Astron. Soc., 482, L46

This paper has been typeset from a TEX/LATEX file prepared by the author.